Published in final edited form as:

Mechanobiol Med. 2025 March ; 3(1): . doi:10.1016/j.mbm.2024.100097.

Increased deformations are dispensable for encapsulated cell mechanoresponse in engineered bone analogs mimicking aging bone marrow

Alexander M. Regner[a,1], **Maximilien DeLeon**[b,c,1], **Kalin D. Gibbons**[a,1], **Sean Howard**[a], **Derek Q. Nesbitt**[e], **Seyedeh F. Darghiasi**[e], **Anamaria G. Zavala**[a], **Trevor J. Lujan**[a], **Clare K. Fitzpatrick**[a], **Mary C. Farach-Carson**[b,c,d], **Danielle Wu**[b,c], **Gunes Uzer**[a,*]

[a]Mechanical and Biomedical Engineering Department, Boise State University, USA

[b]Department of Diagnostic and Biomedical Sciences, UTHealth Houston School of Dentistry, USA

[c]Department of Bioengineering, Rice University, USA

[d]Department of Biosciences, Rice University, USA

[e]Biomedical Engineering Program, Boise State University, USA

Abstract

Aged individuals and astronauts experience bone loss despite rigorous physical activity. Bone mechanoresponse is in-part regulated by mesenchymal stem cells (MSCs) that respond to mechanical stimuli. Direct delivery of low intensity vibration (LIV) recovers MSC proliferation in senescence and simulated microgravity models, indicating that age-related reductions in mechanical signal delivery within bone marrow may contribute to declining bone mechanoresponse. To answer this question, we developed a 3D bone marrow analog that controls

---

[*] Corresponding author. Boise State University, Department of Mechanical & Biomedical Engineering, 1910 University Drive, MS-2085, Boise, ID 83725-2085, USA. gunesuzer@boisestate.edu (G. Uzer).

[1] co-first author.

Ethical approval

This study does not contain any studies with human or animal subjects performed by any of the authors.

CRediT authorship contribution statement

Alexander M. Regner: Writing – original draft, Visualization, Validation, Methodology, Investigation, Formal analysis, Data curation. **Maximilien DeLeon:** Writing – review & editing, Visualization, Validation, Methodology, Investigation, Formal analysis, Data curation. **Kalin D. Gibbons:** Writing – review & editing, Software, Methodology. **Sean Howard:** Writing – review & editing, Visualization, Validation, Supervision, Methodology, Formal analysis. **Derek Q. Nesbitt:** Methodology, Conceptualization. **Seyedeh F. Darghiasi:** Writing – review & editing, Formal analysis, Data curation. **Anamaria G. Zavala:** Supervision, Methodology. **Trevor J. Lujan:** Supervision, Conceptualization. **Clare K. Fitzpatrick:** Supervision, Methodology, Conceptualization. **Mary C. Farach-Carson:** Writing – review & editing, Writing – original draft, Supervision, Resources, Project administration, Methodology, Investigation, Funding acquisition, Conceptualization. **Danielle Wu:** Writing – review & editing, Writing – original draft, Supervision, Project administration, Methodology, Investigation, Funding acquisition, Formal analysis, Data curation, Conceptualization. **Gunes Uzer:** Writing – review & editing, Writing – original draft, Visualization, Validation, Supervision, Software, Resources, Project administration, Methodology, Investigation, Funding acquisition, Formal analysis, Data curation, Conceptualization.

Declaration of competing interest

The authors declare that they have no known competing financial interests or personal relationships that could have appeared to influence the work reported in this paper.

Appendix A. Supplementary data

Supplementary data to this article can be found online at https://doi.org/10.1016/j.mbm.2024.100097.

trabecular geometry, marrow mechanics and external stimuli. Validated finite element (FE) models were developed to quantify strain environment within hydrogels during LIV. Bone marrow analogs with gyroid-based trabeculae of scaffold volume fractions (SV/TV) corresponding to adult (25 %) and aged (13 %) mice were printed using polylactic acid (PLA). MSCs encapsulated in migration-permissive hydrogels within printed trabeculae showed robust cell populations on both PLA surface and hydrogel within a week. Following 14 days of LIV treatment (1 g, 100 Hz, 1 h/day), cell proliferation, type-I collagen (Collagen-I) and filamentous actin (F-actin) were quantified for the cells in the hydrogel fraction. While LIV increased all measured outcomes, FE models predicted higher von Mises strains for the 13 % SV/TV groups (0.2 %) when compared to the 25 % SV/TV group (0.1 %). While LIV increased collagen-I volume 34 % more in 13 % SV/TV groups when compared to 25 % SV/TV groups, collagen-I and F-actin measures remained lower in the 13 % SV/TV groups when compared to 25 % SV/TV counterparts, indicating that both LIV-induced strains and scaffold volume fraction (i.e. available scaffold surface) affect cell behavior in the hydrogel phase. Overall, bone marrow analogs offer a robust and repeatable platform to study bone mechanobiology.

Keywords

Mechanical signals; Low-intensity vibration; Mesenchymal stem cells; 3D printing; Mechanical modeling; Tissue modeling

1. Introduction

Mesenchymal stem cells (MSC) found in adult musculoskeletal tissues maintain tissue turnover and repair. In bone, MSC is the common progenitor for osteoblasts, osteocytes and adipocytes.[1-3] During habitual loading, MSCs provide necessary osteoblast populations to facilitate bone modeling.[4] Aging[5-7] and chronic unloading under microgravity[8,9] decrease exercise-induced bone accrual. While aging and unloading phenotypes are associated with decreased proliferative and osteogenic differentiation capacity of MSCs,[10,11] findings from *in vitro* replicative senescence[12] and simulated microgravity models[13] show that exposing MSCs to mechanically active environments improve these outcomes. *In vivo* studies using long daily treadmill activity[14] or ladder climbing regimens[15] report improved MSC function with long-term physical activity. These studies suggest that trabecular volume may contribute to declining bone mechanoresponse in aging and prolonged unloading scenarios. To this end, we sought to develop a 3D bone marrow analog to study the role of trabecular bone volume on MSC function and quantify the effects of trabecular bone volume on MSC mechanoresponse under external mechanical stimulation.

MSCs in bone exist in a mechanically rich environment. Inside the bone marrow, bone surfaces where bone cells reside, are exposed to matrix deformations,[16-19] accelerations,[20-25] fluid flow,[26-30] and changes in intramedullary pressure,[31-33] all of which are inseparable.[34] Cyclic bone deformations associated with walking, for example, generates strains up to 400$\mu\varepsilon$ and fluid velocities up to 100 μm/s within the lacunar–canalicular network.[35] When looking for candidate loading regimens for the bone marrow analog model, we determined that vibration is the most applicable and practical mechanical input. When a person runs, tibial accelerations reach 2–5 g[36] (1 g = 9.81 m/s^2), creating complex loading conditions[37] capable of driving MSC function.[38] High frequency and low magnitude signals are part of bone physiology; measuring 24 h strain history of load bearing bones across different species showed that bones are subjected to thousands of very small, high frequency strains ($< 10\mu\varepsilon$) during the day.[39] Leveraging the presence of these small strains, application of low intensity vibration (LIV), usually applied between 30 and 100 Hz with acceleration magnitudes of 0.1–1 g, have been used in clinical, pre-clinical and cellular studies.[4] In clinical studies, LIV protects bone quantity and quality in women with osteoporosis,[40,41] children with cerebral palsy,[42] and improves bone indices in child cancer survivors.[43] Animal studies demonstrated that external LIV application increases trabecular bone density and volume,[20] creates stiffer bones,[44] and improves disuse-induced bone loss.[45] At the cellular level, our group reported that application of LIV increases MSC contractility,[46] activates RhoA signaling,[47] and results in increased osteogenic differentiation and proliferation of MSCs.[48] Similar to other mechanical signals such as substrate strain, LIV increases the nuclear accumulation of mechanically-sensitive transcription factors, β-catenin[49] and YAP[50] as well as increasing nuclear stiffness.[51] We recently reported that in a simulated microgravity model where MSCs were exposed to rotating cell culture vessels for 72 h to simulate gravitational unloading, LIV rescued YAP nuclear entry induced by RhoA-activator lysophosphatidic acid.[50]

The mechanical environment LIV generates within the bone marrow is not well studied due to a lack of repeatable model systems. Early modeling efforts utilizing idealized rectangular bone lattices[37] or realistic bone geometries from μCT scans of a human lumbar vertebra[52] reported that LIV can generate fluid shear stress on bone surfaces up to 1–2 Pa depending on the bone marrow viscosity. Follow-up *ex vivo* studies that combined computational modeling with trabecular explant models under 0.3 g, 30 Hz LIV showed that LIV-induced fluid shear was, in part, correlated with histological findings. However, fluid shear stress levels alone were unable to explain all the findings. For example, application 0.9 ml/min fluid flow elicited a lower response when compared to LIV,[53] suggesting that other mechanical or geometrical factor plays a role in regulating cellular response. Supporting these findings, our group further reported that during osteogenic differentiation of MSCs[48] LIV signal that generated 0.04Pa of fluid shear stress (0.15 g, 100 Hz) resulted the same mineral deposition when compared to LIV signals that generated fluid shear stress of 0.27Pa (1 g, 100 Hz) and 0.94Pa (1 g. 30 Hz). Similar insensitivity of osteoblasts[54] and osteocyte[55] signaling to LIV-induced fluid shear stress indicated that LIV may act though multiple pathways to affect cell behavior While previous studies reveal possible LIV mechanisms, there are no current *in vitro* models to capture the mechanical complexity of bone marrow during mechanical stimulation. Consequently, biological variation and sample availability makes it challenging to setup robust *ex vivo models* to study the effect of trabecular bone volume using multiple outcomes from identical conditions.

Therefore, to overcome these challenges, we developed a cell-laden bone marrow analog with a 3D printed PLA trabeculae and hyaluronic acid-based bone marrow to quantify the effects of trabecular-like scaffold volume on MSC response during LIV. The hydrogel strains created during 1 g, 100 Hz vibrations in both 13 % and 25 % scaffold bone volumes

– representing bone volumes of 64 week old (aged) and 8 week old (young) adult male C57BL/6 J mouse – were compared.[56] Both validated finite element (FE) simulations and *in vitro* experiments were used to determine whether trabecular-like scaffold volume affects the scaffold mechanical environment and MSC response.

1.1. Experimental design

To create a validated experimental bone-analog model, PLA was chosen for the material of the trabecular structure due to its biocompatibility[57] and ease of use in 3D printing applications.[58] Previously developed hyaluronic acid-based hydrogels with MMP cleavable crosslinks and cell attachment sites were chosen to model bone marrow.[59] Primary mouse MSCs dispersed in hydrogels were used as the cell model due to their versatility in both proliferative and differentiation experiments utilized in previous studies.[13,16,20,44,45,47-50,60] To generate an experimentally validated FE model we first utilized a collagen-based gelatin hydrogel (i.e., calibration gels) followed by hyaluronic acid (HA) hydrogel experiments to set model parameters. To define hydrogel material properties for the FE model calibration we employed high-speed compression tests and high-speed speckle photography analysis. Due to large difference in elastic modulus between bone marrow and trabecular bone,[57,61,62] PLA scaffolds were assumed to be rigid for the purposes of the FE model. Following FE model calibration, idealized 3D trabecular structures based on gyroid model[63] with either 13 % or 25 % volume fill (i.e. scaffold volume) were generated and LIV-induced HA hydrogel strains were compared between the two trabecular volumes (Fig. 1a). For *in vitro* experiments (Fig. 1b), we encapsulated 13 % and 25 % PLA scaffolds with HA hydrogel-MSC mixture using 1 million cells per mL of hydrogel. Cell-laden hydrogels with no PLA scaffold were used as no-scaffold controls (referred as 0 %). Cell-laden 13 % and 25 % scaffolds were exposed to LIV vibration 1 h every day at room temperature using 100 Hz frequency and 1 g acceleration magnitude using protocols we established previously.[48] While our experiments did not use osteogenic media formulations, we selected 14 days as our time point to understand cellular response within timescales required for *in vitro* osteogenic differentiation.[64] After 14 days, samples were allocated for mRNA (N = 4/group), immunostaining (N = 3/group). Controls were handled the same but were not vibrated. Both RNA and imaging measurements were collected from the hydrogel fraction.

2. Methods and materials

2.1. Preparation of hydrogels for mechanical testing and calibration

Calibration gels (Knox unflavored Gelatin) or HA hydrogels (Advanced Biomatrix: GS1004) were prepared in 3D PLA printed cylindrical molds with a diameter of 24 mm and a height of 9 mm (Fig. 1c). The calibration gels were prepared at 2 mg/ml via dissolving the gelatin powder in 50 °C water. Sample molds used for calibration gels were lined with a thin layer of petroleum jelly to improve mold release and 4.1 ml of 2 mg/ml gelatin mixture was pipetted in. Filled molds were cooled over ice for 1 h to cross-link and then both the gel and mold were deposited into a room temperature water bath for 30 min. The calibration gel samples were carefully removed from the molds and tested. All tests were completed within 3 h of initial calibration gel deposition into the molds. HA hydrogels were prepared according to manufacturer protocols. Briefly, degassed (DG) water was extracted via syringe and added to the Glycosil (5.0 ml DG water) and Extralink-Lite (2.5 ml DG water). These were vortexed on a rocker for 60 min and vigorously shaken by hand every 15 min. These solutions then were combined in a 4:1 ratio (v/v) and mixed by pipette into the mold. These gels cross-linked for 90 min at room temperature, removed from the mold, deposited into PBS in 90 mm well plate (VWR#10062–878) sealed with parafilm, and left overnight in a 37 °C in an incubator, and. The next day the HA hydrogels were tested one at a time, removing them from the PBS immediately prior to testing.

2.2. Instantaneous compression testing

Instantaneous compression testing was performed using an INSTRON ElectroPuls E10000 using a 10 N load-cell attached to a loading plate with a diameter of 35 mm. At the start of each test, calibration and HA gels were placed on water-coated Teflon sheets to prevent adherence (Fig. 1c). Samples were pre-loaded with 0.025 N to ensure full contact with the plate, then compressed to 20 % strain (compared to pre-loaded gauge length) at a rate of 90 mm/s. Loading plate position then was held constant for 100 s and load-cell data was collected and exported into an excel sheet. The 100 s relaxation data was fitted using a 2-term exponential decay function $[f(x) = ae^{bx} + ce^{dx}]$ representing viscoelastic material relaxation (Fig. 1d). Next, instantaneous force and displacement data was collected during 20 % compression at a rate of 10.8 mm/s. Compression data was entered into MATLAB, converted to engineering stress and engineering strain, and then fit using a 5th order polynomial $[f(x) = ax^5 + bx^4 + cx^2 + dx^2 + ex + f]$ representing the instantaneous material behavior (Fig. 1e). Stress–strain curves for the calibration and HA gels are provided in Supplementary Fig. S1.

2.3. Digital image correlation tests

Prepared calibration gels were tested in wells with differing width for FE model validation. Shown in Fig. 2a, wells with fixed depth (9 mm) and height (27.5 mm, Y direction) were 3D printed out of PLA for widths of 4 mm, 5 mm, 6 mm, and 8 mm (X direction). These wells were filled with calibration gels as described above and then were speckled with a 50/50 mixture of talc powder and grid 220 silicon carbide (SiC) to track their motions via speckle photometry as previously described[18]. To track light-reflective siC speckles, a white LED light source was used and the motion of the surface was captured with a Photron UX50 high-speed camera at a rate of 2000 frames per second (fps). PLA wells filled with calibration gels were vibrated horizontally along the X-direction at 100 Hz with an acceleration of 1 g via a custom-made vibration bioreactor driven by a Labworks ET-126HF-1,-4 (13lbf) Electrodynamic transducer using a sinusoidal driving function (Fig. 2a). All vibration tests were performed within 3 h of gel casting. Recording of gel motion was started 15 s post-LIV to ensure that steady state was reached. Recorded high speed videos at 2000fps were analyzed using digital image correlation (DIC) with NCORR software[65] (V1.2) to export gel displacements relative to a moving frame of reference marked on the well surface. Post-processing of the full-field displacement maps were performed in MATLAB. Vibrations were applied along the x-axis and the well height direction was referred as y-axis (Fig. 2b). During the post-processing of the vibration experiments, the ε_{xx} strain was exclusively analyzed, as it was found to be at least one order of magnitude larger than ε_{yy} or ε_{xy} (see

Fig. S2). For HA gel experiments, only the 8 mm well width was used and same steps were repeated as above. All experiments were performed in triplicate.

2.4. Finite element model generation and validation

A pre-processing software package (*Hypermesh v2017.2, Altair, MI*) was used to generate meshes for finite element analysis. 3D printed well geometries between 4 and 8 mm were imported as STL files and converted to rigid R3D4 mixed elements. The hydrogels were meshed using hexahedral C3D8R elements with a size of 0.25 mm. These meshes were imported into a FE solver (*ABAQUS R2019x, Simula, RI*) to simulate vibration. The hydrogel material was modeled with a density of 1.0023 g/cm^3 for calibration gels and a density of 1.0018 g/cm^3 for HA gels. Hyper-viscoelastic material responses were modeled using the procedure outlined by Dalrymple[12]. For viscoelastic modeling, the long-term relaxation was measured starting from the end of the instantaneous compression to a 100 s interval. This then was fit using a second order exponential function, and data was extrapolated back to 10^{-4} s to ensure that input data to the finite element simulation was within the rate of vibration (100 Hz). For viscoelastic material definition a single-term Ogden model with three-term Prony Series was used.[66] The elastic material definition was modeled as hyperelastic with a 5th order Ogden fit, $U = \sum_{i=1}^{N} \frac{2\mu_i}{\alpha_i^2}\left(\lambda_1^{-\alpha_i} + \lambda_2^{-\alpha_i} + \lambda_3^{-\alpha_i} + \lambda_4^{-\alpha_i} + \lambda_5^{-\alpha_i} - 5\right) + \sum_{i=1}^{N} \frac{1}{D_i}\left(J^{el} - 1\right)^{2i}$ where λ_i are principal stretches, N is a parameter (in this case equal to 5), μ_i, α_i, and D_i are temperature dependent material parameters. These materials were defined within the FE solver using the instantaneous, uniaxial test data (Fig. 1e).

The material interaction between the undeformable and hydrogel parts used a linear press-overclosure with a slope of 1.0×10^{-2} and a friction and damping coefficients that minimized the difference between experimental and numerical ε_{xx} strain magnitudes at timepoint $\pi / 2$ using a design of experiments optimization as described below. Mechanical vibration was applied using a connector actuator driven by a periodic velocity equation with an amplitude of 15.61 m/s, and a circular frequency of 100 Hz (628.31 radians).[54]

2.5. Damping and friction coefficient optimization

The root mean square error (RMSE) between the time dependent FE displacement output and the DIC experimental data were calculated using the ε_{xx} surface strain at the $\pi / 2$ timepoint of the 8 mm well width. To calibrate the friction and damping coefficients in the FE model, a 3 factor 3 level design of experiments (DOE) was performed starting from the measured stiffness value. For the friction and damping coefficients, we started with ABAQUS recommended defaults values of 0.75 and 0.03, respectively. The stiffness value for the calibration gels varied ±50 % of the measured value and the friction and damping coefficients varied between 0.1 −10 and 0.03–0.3, resulting in 27 simulations (Table 1). For each comparison, the gel surface was divided into a 15 × 37 grid and for each sub-region the RMSE difference between the experimental and computational ε_{xx} strains were compared. Following this analysis, the friction and damping coefficients that minimized the RMSE response were selected (Fig. 2f). Because increasing or decreasing stiffness from the measured values always resulted in larger RMSE values, 2 factor 3 level DOE was used for the HA gels (Table S1) and the friction and damping coefficients that minimized the RMSE response were selected (Fig. S3).

2.6. Scaffold finite element modeling

Scaffolds were generated using two bone volumes, 13 % and 25 %, respectively corresponding to bone volumes of 8 week old (young) or 64 week old (aged) male C57BL/6 J mice.[67] Gyroid geometries representing trabecular structures were generated using the equation: $sin(x)cos(y) + sin(y)cos(z) + sin(z)cos(x) < t$, where t is a constant linearly related to the percent volumes.[63] For 13 % and 25 %, the t scaling value used was −0.121 and −0.752. These models were generated using *MathMod v8.0*, meshed in *Adobe MeshMixer v3.5* using a cell surface density of 128. The models then were scaled to final dimensions of, 5 mm × 5 mm x 10 mm. These then were exported to *Altair Hypermesh v2017.2,* where the STL models were meshed using mixed elements with an element size of 0.14 mm. Meshes were made into solid C3D4 elements using tetramesh. The surface of R3D3 elements were exported into ABAQUS.

The FE model was simulated in *ABAQUS (R2019x, Simula, RI)*. Pressure-overclosure with a slope of 1.0×10^{-2} was applied to ensure contact between the scaffold and hydrogel surfaces, and both the surface damping and friction coefficients were taken from the optimization procedures. Similar to the previous simulations, the rigid bone was driven by a connector actuator using a periodic velocity equation with an amplitude of 15.61 m/s, and a circular frequency of 100 Hz (628.3 radians). The volumetric strain components corresponding to 13 % and 25 % scaffolds (ε_{xx}, ε_{yy}, ε_{zz}, ε_{xy}, ε_{yz}, ε_{zx}) were exported. The total hydrogel strain magnitude approximated via equivalent von Mises strain $\varepsilon_{eq} = 2/3\sqrt{3(e_{xx}^2 + e_{yy}^2 + e_{xx}^2)/2 + (\gamma_{xy}^2 + \gamma_{yz}^2 + \gamma_{zx}^2/4}$, where engineering strains defined as $\gamma_{ij} = 2\varepsilon_{ij}$ and deviatoric strains defined as

$$e_{xx} = +1/2\varepsilon_{xx} - 1/3\varepsilon_{yy} - 1/3\varepsilon_{zz}, e_{yy} = -1/3\varepsilon_{xx} + 2/3\varepsilon_{yy} - 1/3\varepsilon_{zz},$$
$$e_{zz} - 1/3\varepsilon_{xx} - 1/3\varepsilon_{yy} + 2/3\varepsilon_{zz}.$$

2.7. Scaffold fabrication and application of low intensity vibration

STL files of the 13 and 25 % gyroidal scaffolds were 3D printed using PLA on a PRUSA Mk3s 3D printer (PRI-MK3S-KIT-ORG-PEI) with 0.1 mm layer height, and 0.5 × 0.5 × 1cm overall outer dimensions. Scaffolds were sterilized with ethylene oxide autoclave prior to cellular encapsulation.

HA hydrogels were functionalized with integrin binding motifs (acrylate-PEG-GRGDS) to encourage cell adhesion and metalloproteinases (MMPs)-sensitive crosslinkers (acrylate-PEG-PQ-PEG-acrylate) to allow cells to modify the hydrogel during growth and cell network formation.[68] Cells mixed into the hydrogel at 1×10^6 cells/ml prior to casting into scaffolds and cross-linking. Cell seeded hydrogels were kept for 7 days in growth media in 5 % CO_2 and 37 °C to allow growth and attachment prior to experimentation. After 7 days, scaffolds were transferred to two 6 well plates (Corning#3516) with Growth Media (IMDM, 10 % (v/v) FCS and 1 % (w/v) pen-strep). Scaffolds were oriented identically to the 3D print, and with the long axis orthogonal to the axis of vibration. Scaffolds were secured with a custom 3D printed PLA top and one 3D printed 30 mm PLA platen attached to a stainless-steel screw threaded through the top in each well (Fig. 4a). These ensured the scaffolds would not move during vibration. The scaffolds vibrated for 1 h each day for 14 days.

2.8. Immunostaining, hydrogel imaging and analysis

Samples were rinsed twice in PBS fixed using 4 % (v/v) paraformaldehyde for 15 min at room temperature. Next, they were rinsed 2 times for 5 min in PBS before being permeabilized in 0.1 % Triton/PBS (v/v) for 15 min at room temperature. All further steps have a 3 × 10 min rinse in PBS between them. The scaffolds were stained against collagen-I (*Bioss Antibodies #bs-10423R-A594)*. Based on antibody species, fixed cells blocked using appropriate serum for 30 min at room temperature, stained with primary antibody for 1 h at 37 °C and labeled against F-actin (1:60 in PBS *Alexa Fluor® 488 Phalloidin-Invitrogen,* # A12379) and DNA (NucBlue, 2 drops/ml, Fisher Scientific #R37605). After a final two rinses for 5 min each, the scaffolds were imaged using A1R/MP + Confocal/Multiphoton Microscope (Nikon Instruments). Since our goal was to evaluate the cells within the hydrogel fraction, we imaged the hydrogel regions free of scaffold surfaces. At least five regions of interest (ROI) were selected and z-stacks acquired (100 × 600 × 600 μm) (Fig. S6). Imaris image quantification software (Oxford Instruments) was used to quantify fluorescence micrographs. Quantification of cellularity was based on nuclear staining (NucBlue) using *Spots* functionality in Imaris. This feature accurately counts nuclear objects in 3D spaces. Total F-actin (Fig. 5, Fig. S7) and collagen-I volumes were quantified using *Surfaces* functionality and average volume of each detected surface was reported per ROI. *Surfaces* reports volume of geometries in 3D fluorescence micrographs so comparisons may be performed in all experimental conditions. Changes in morphology and irregular geometries are achievable using this mode of quantification.

2.9. RNA isolation and assessment of transcript levels

To match imaging data, each scaffold was centrifuged at 3000 rpm to separate the gel and scaffolds to quantify RNA expression on the hydrogel fraction. Separated gels were added to a single 2 ml tube, and TRIzol™ (*Fisher Scientific#15-596-026*) was added. Gels were mechanically broken up for 30 s with a P1000 micropipette and the scaffolds that had been spun to remove the gel were suspended in Zymo lysis buffer and frozen at −80 °C overnight. The RNA then was extracted according to manufacturer's protocols (Zymo Research #R2071). These RNA samples then were converted to cDNA and PCR analysis was performed for collagen-I transcripts using 18 S as the control gene. Reverse transcription was performed with 1 μg RNA in a total volume of 20 μl per reaction. 25 μL amplification reactions contained primers at 0.5 μm, deoxynucleotide triphosphates (0.2 mm each) in PCR buffer, and 0.03 U Taq polymerase along with SYBR-green (Molecular Probes, Inc., Eugene, OR) at 1:150,000. mRNA levels were compared using ΔΔCt method as previously reported.[48] Samples were analyzed in triplicate. PCR products were normalized for the amount of 18 S amplicons. The following primers were used for 18 S (Forward-GAACGTCTGCCC TATCAACT, Reverse-CCAAGATCCAACTACGAGCT) and collagen-I (Forward-ATGTGCCACTCTGACTGGAA, Reverse-CAGACGGCTGAGTA GGGAA) transcripts.

2.10. Sample statistics

Results were presented as mean ± standard deviation. Immunostaining and qPCR analyses were performed using samples from three or more independent experiments. As we reported,[13,49] for comparisons regarding qPCR, differences among treatments within each biological replicate were assumed to follow a normal distribution due to large mean sample size (20,000 or more cells/group), thus for these comparisons, we used two-tailed un-paired one way ANOVA followed by Newman–Keuls post-hoc tests. For other comparisons with smaller sample sizes, including imaging experiments, we used non-parametric two-tailed Mann–Whitney U-test or Kruskal–Wallis test; p-values of less than 0.05 were considered significant. Statistical analyses were performed using Prism v.10 (GraphPad Software).

3. Results

3.1. Lateral strain positively correlates with distance during low intensity vibration

High speed visualization of wells horizontally vibrating on X-direction at 100 Hz frequency and 1 g acceleration magnitude (Fig. 2b) showed that the maximum lateral ε_{xx} strain, measured at the peaks of the cycle ($t = \pi / 2$ & $t = 3\pi / 4$), reached to 0.014 ± 0.00047 at 8 mm spacing over 5 cycles when averaged across three experiments. The maximum ε_{xx} values were symmetrical on both ends of the well, ensuring that steady state was achieved during measurements (Fig. 2c). Minimum strains were measured at the end of each positive stroke ($t = \pi$). Compared to 8 mm at $\pi / 2$ & $t = 3\pi / 4$ timepoints, averaged maximum ε_{xx} strains of 6 mm, 5 mm, 4 mm well widths were decreased to 0.00806 ± 0.00050 (−0.86 %, $p = 0.66$), 0.0075 ± 0.00047 (−7.6 %, $p = 0.17$), 0.0030 ± 0.00014 (−62 %, $p < 0.05$), respectively (Fig. S4a). The $\pi / 2$ sets for each spacing over all three trials were collated into data distribution plots to show the ε_{xx} strains as a function of distance from the well wall (Fig. S4b).

3.2. Differences between experimental and computational lateral strains are affected by material stiffness and friction and damping coefficients

Prior to validating the FE model, we first optimized the model parameters using the experimental data from the 8 mm well width experiments. The effect of material stiffness on the average RSME match between DIC experiments and FE models was quantified using the averaged ε_{xx} distribution at the positive and negative peaks (Fig. 2d). The maximum ε_{xx} values were symmetrical at both the $\pi / 2$ and $t = 3\pi / 4$, in addition to both ends of the well, demonstrating steady state (Fig. 2e). Using experimentally measured stiffness and FE software default values of 0.75 and 0.03 for the friction and damping coefficients, the average RSME between DIC and FE at $\pi / 2$ timepoint was 0.19 while the average RMSE between experimental replicates (among the three wells) was 0.15, showing that the average mismatch between FE and DIC was within experimental error. Using default friction and damping coefficients, increasing or decreasing the measured material stiffness by 50 % resulted in average RMSE values of 0.36 and 0.63, which were larger than the experimental variation and indicated the importance of accurate stiffness measurements for modeling.

Because the exact boundary conditions between the gels and the PLA were unknown, we investigated the possible combinations of friction and damping coefficient values that could further minimize the average RMSE values. Varying the friction coefficient between 10 and 0.1 resulted in the average RMSE values of 0.28 and 0.16 at measured stiffness and default damping coefficient. Similarly, only varying damping coefficient between values of 0.3 and 0.003 resulted in average RMSE values of 0.28 and 0.3, respectively. Using the experimentally measured mechanical properties, an empirical linear DOE model using a 2nd order polynomial determined the optimal friction/damping combination (Table 1). The lowest average RMSE of 0.16 was obtained at the friction/damping combination of 0.1/0.003. Shown by the 15 × 37 RMSE grid (Fig. 2e), maximum differences between the experimental- and FE-derived ε_{xx} magnitudes were largest near the outer walls. Of this, the largest RMSE difference of 0.015 occurred in regions 5 and 6. Match in regions 3 and 4 was closer, an averaged difference of 0.0047 and 0.0052, respectively. Differences in corner regions 1, 2, 5 and 6 were 0.0077, 0.0079, 0.0113, and 0.0122, respectively. RMSE grid for the HA gels is shown in the Supplementary Fig. S3. The largest RMSE difference of 0.024 again occurs in region 6, with regions 3 and 4 (the middle regions) matching the closest with ε_{xx} averages of 00.0091 and 0.0082, respectively. Differences in corner regions 1, 2, 4, & 5 were 0.011, 0.010, 0.010, and 0.098, respectively.

Using the friction/damping coefficient combinations that minimized the average RMSE values between DIC and FE results at 8 mm well width, we quantified the averaged ε_{xx} magnitudes over 6 mm, 5 mm, and 4 mm for the calibration gel. The $\pi/2$ sets for each spacing over all three trials collated into data distribution plots (Fig. S4c), which showed increasing extrema differences as the spacing decreased from 8 mm. When compared to 8 mm, the averaged maximum ε_{xx} strains of 6 mm, 5 mm and 4 mm well widths decreased to 0.017 ± 0.00040 (−22 %, $p < 0.05$), 0.013 ± 0.00030 (41 %, $p < 0.05$), 0.010 ± 0.00037 (−54 %, $p < 0.05$), and 0.0026 ± 0.00051 (−88 %, $p < 0.05$), respectively. Plotting ε_{xx} strains as a function of distance from the well wall showed increasing strain values with larger cavities (Fig. S4d).

3.3. Low scaffold volumes increase LIV-induced hydrogel strains

We next compared the 3D strain distribution between 13 % and 25 % scaffolds under LIV (Fig. 3a) using HA gel mechanical properties. Comparing the Von Mises strain (ε_{VM}) magnitude averaged over steady–state cycles showed that ε_{VM} of 25 % was 50 % smaller compared to 13 % scaffold (Fig. 3b, $p < 0.0001$). ε_{VM} distribution (Fig. 3c) indicated normally distributed strains for both 13 % and 25 % scaffolds. Histograms of 25 % and 13 % scaffolds were statistically different ($p < 0.05$), 25 % scaffolds had more elements with lower strain values, while 13 % scaffolds showed elements with higher ε_{VM} strains. Comparing individual strain components showed a significant difference ($p < 0.05$) between ε_{zz}, ε_{xy} and ε_{yz} strains, no differences were found between ε_{xx}, ε_{yy}, and ε_{zx} strains. Min/Max values for the normal (εxx, ε_{yy} and ε_{zz}) and shear (εxy, ε_{yz} and ε_{zx}) components are provided in Table 2.

3.4. LIV increases cellularity and F-actin volume in the hydrogel fraction

In order to compare the possible differences in MSC mechanoregulation due to scaffold volume differences we generated two sets of PLA scaffolds (13 % and 25 % volume fill) and 0 % controls. Cell-laden 13 % and 25 % scaffolds vibrated 1 h every day at room temperature using 100 Hz frequency or 1 g acceleration magnitude (Fig. 4a). During vibrations, controls were kept outside of the incubator but were not vibrated. After 14 days, samples were allocated for qPCR (N = 4 scaffolds/group), imaging (N = 3 scaffolds/group). Live/dead straining prior to start of the experiments at day 0 (7 days post-encapsulation) showed viable cells on both PLA and in hydrogels (Fig. 4c). Shown in Fig. 4d, morphology of cells on PLA surfaces were similar to 2D culture plates (Fig. S5), showing an elongated and flattened morphology, while cells in hydrogels were rounded with dendritic extensions (Fig. 4d). However, due flat cell morphology and difficulties in reliably quantifying the cell numbers on scaffold surfaces and between ridges, we quantified the cellularity within equal volumes of hydrogel fractions avoiding scaffold regions (Fig. S6). By counting cell nuclei per imaging field 13 % and 25 % scaffolds on average had 61 ± 35 and 49 ± 35 cells (Mean ± STD), respectively and were not statistically different from each other. Application of LIV increased the cell number to 91 ± 47 in 13 % scaffolds which was not significant compared to no-LIV control. LIV increased cell count to 94 ± 67 per imaging area for 25 % scaffolds ($p < 0.05$).

We next tested the F-actin volume in hydrogels in response to LIV using samples stained against Phalloidin. Comparing 0 %, 13 % and 25 % samples without LIV showed no significant change in the F-actin volume. Shown in Fig. 5c, comparing −LIV samples with their +LIV counterparts we found that 13 % SV/TV group with a larger hydrogel strain (average ε_{VM} 0.2 %, Fig. 3b) had a trend toward increasing F-actin (+50 %, ns) while 25 % SV/TV with a lower hydrogel strain (average ε_{VM} 0.1 %, Fig. 3b) showed a 2.4-fold increase ($p < 0.05$). Normalizing the F-actin data to number of nuclei per ROI did not change the outcome (Fig. S7).

3.5. Scaffold volume differentially regulates basal and LIV-induced Type-I collagen production

Collagen-I immunostaining showed a more robust collagen labeling in vibrated samples (+LIV), when compared to non-vibrated controls (−LIV, Fig. 5d-e). Collagen-I mRNA quantification showed a trend of increased collagen-I levels in +LIV samples (+50 % in 13 % and +94 % in 25 % samples, Fig. 5f). Quantification of collagen-I from volumetric scans showed unchanged basal collagen-I levels between 0 % and 13 % controls while -LIV 25 % group had a 73 % increase compared to -LIV 13 % group ($p < 0.05$). LIV increased collagen-I in both 13 % and 25 % groups by 87 % and 53 % respectively ($p < 0.01$) and +LIV 25 % remained significantly higher compared to + LIV 13 % group (37 %, $p < 0.05$).

4. Discussion

We found that hydrogel strain magnitudes between scaffolds representing young (25 %) and aged (13 %) scaffold volumes significantly differ during LIV. Validation studies indicate that strain magnitude within the LIV direction is positively correlated with the spacing between two solid structures (Fig. 3d & S4). This conclusion was supported when comparing 25 % and 13 % scaffolds: Average ε_{VM} for the 25 % scaffold was 50 % smaller when compared to the 13 % scaffold which had more spacing between trabecular struts (Fig. 3a-b). These findings indicate that age-related bone adaptations, decreased trabecular volume and increased cortical circumference[56] may serve to increase the magnitude of bone marrow deformation during physical activity. LIV increased collagen-I volume in both 13 % and 25 % groups by 87 % and 53 % respectively ($p < 0.01$). In this way, 13 % scaffolds showed 34 % more collagen-I volume when compared to 25 % scaffolds. Thus it is possible that the difference is due to increased strains in 13 % scaffolds (~50 % more von Mises strains). In contrast to larger hydrogel strains, observed F-actin volumes (Fig. 5a-c) and collagen-I production (Fig. 5d-g) of 13 % scaffolds were lower when compared to 25 % scaffolds under LIV. Given that LIV-induced cellularity (Fig. 4e) as well as F-actin (Fig. 5c) did not show larger changes in 13 % scaffolds, we conclude that LIV response was in-part insensitive to hydrogel strains. This insensitivity of LIV response in hydrogels can be attributed to several factors. First, measured strain differences within the hydrogel only represent a fraction of the mechanical information. During 1 g, 100 Hz sinusoidal vibrations the entire scaffold, including PLA surfaces and hydrogel, accelerates and decelerates to speed of ±15 mm/s, 100 times each second, providing another mechanical input in addition to LIV-induced hydrogel strains. We previously reported that when substrate strains are extremely low, LIV activates COX-2 signaling in MC3T3 osteoblasts,[54] improves gap junctional communication in MLO-Y4 osteocytes[55] and increases proliferation as well as biosynthesis of collagen and related proteins in MSCs under simulated microgravity.[13] While this suggests that LIV could regulate collagen production and changes in F-actin that are independent of hydrogel strains, the finding that 25 % scaffolds produce more collagen when compared to 13 % scaffolds and 0 % controls indicates that loss of scaffold volume could negatively affect the function of the MSCs inside the hydrogel.

A possible reason for increased collagen production is the difference in scaffold surface area. Based on our measurements from the STL files, 13 % scaffold to total volume (SV/TV) had a surface area of 106.2 mm^2 surface area and 25 % SV/TV scaffolds had a 152.538 mm^2 surface area. Due to increased scaffold volume, the 25 % scaffolds had a smaller hydrogel volume, increasing the possibility that imaging regions are closer to the scaffold walls. Confocal images showed many cells that were viable and spread on the PLA surfaces (Fig. 4d). While our analysis excluded cells on the PLA surface from the data, these cells on PLA surfaces are likely to produce paracrine signals to cells within the hydrogels. For example, during bone remodeling, early stage osteoblast lineage cells that reside on bone surfaces are at a low cell density, but their density increases during the reversal phase.[69] Interestingly, early osteoblast lineage cells are “pro-resorptive” and osteoid deposition starts only when a critical cell density is reached.[70] This suggests that basal and LIV-driven density changes of these PLA surface cells could not only signal to hydrogels cells, but also could regulate important factors such YAP/TAZ that change their subcellular localization based on cell density.[71] While the metrics of this population were not investigated in this study, future studies aimed at possible interactions of cells on the PLA surface and hydrogel will be critical to identify the interactions between scaffold adherent and non-adherent cell populations.

Despite our attempts to calibrate material parameters in the FE model based on experimental data, differences between our DIC experimental data and our FE model data were seen in both calibration and HA gels. Highlighting the inherent variation in DIC experiments, the average RMSE values between calibration or HA experiment were close to differences between experimental data and computational models. Several factors could have contributed to this variability. The first relates to the rigid body assumption we assigned to PLA in our simulations. While this appears to be a reasonable assumption and used by others,[57] a potential model limitation is the inability to account for strain damping from the walls, which could decrease the wall strain in the FE model. Another source of error is the DIC method itself, where the PLA-hydrogel boundaries cannot be resolved via optical resolution, resulting in lower averages at the boundaries when compared to FE model, where element size was 250 μm. While, this limitation of DIC could underestimate the magnitudes towards the walls, FE model did predict the relative differences observed experimentally among different well sizes, and therefore the relative differences predicted by the model between the two scaffold volume fractions remains credible. 250 μm element size was adequate to validate the speckle measurements. Since we are reporting averaged strains per scaffold (Fig. 3), but not cellular strains experienced by each cell, we concluded that this element size was appropriate. Additionally, given the increased cellularity in 25 % scaffolds under LIV (Fig. 4e), it is possible that hydrogel mechanical properties degrade faster, resulting in different strains from what our study predicted using the gel mechanical properties pre-experimentation. Finally, our 3D printed scaffolds are approximation of trabecular structures and do not recapture disconnections in trabeculae *in vivo*.

In this study, we developed bi-phasic bone analogs with a fully characterized hydrogel strain environment during LIV. Our findings showed that scaffold volumes associated with trabecular densities of advanced age resulted in higher hydrogel strains, while trabecular densities expected at adulthood resulted in smaller strains during LIV. Despite the lower strain magnitudes, hydrogels mimicking young bone marrow supported higher F-actin measures and collagen production in both basal and mechanically stimulated scaffolds, indicating that factors other than hydrogel environment are in play. These findings not only reveal interesting new avenues of research to study interactions between scaffold-lining and hydrogel encapsulated cells to mimic bone marrow mechanobiology, but the model itself establishes a versatile 3D platform to study how mechanical signals may affect multicellular processes such as environmental factors, aging, inactivity, microgravity and radiation.

Supplementary Material

Refer to Web version on PubMed Central for supplementary material.

Acknowledgements

This work was supported by the National Institutes of Health (R01AG059923), P20GM109095, and 5P2CHD086843-03) and National Science Foundation (1929188 and 2025505).

Data availability

The datasets generated and/or analyzed during the current study are available from the corresponding author on reasonable request.

References

1. Krishnan V, Bryant HU, MacDougald OA. Regulation of bone mass by Wnt signaling. J Clin Invest. 2006;116(5):1202–1209. [PubMed: 16670761]
2. Menuki K, Mori T, Sakai A, et al. Climbing exercise enhances osteoblast differentiation and inhibits adipogenic differentiation with high expression of PTH/PTHrP receptor in bone marrow cells. Bone. 2008;43(3):613–620. [PubMed: 18567552]
3. David V, Martin A, Lafage-Proust MH, et al. Mechanical loading down-regulates peroxisome proliferator-activated receptor gamma in bone marrow stromal cells and favors osteoblastogenesis at the expense of adipogenesis. Endocrinology. 2007;148(5):2553–2562. [PubMed: 17317771]
4. Pagnotti GM, Styner M, Uzer G, et al. Combating osteoporosis and obesity with exercise: leveraging cell mechanosensitivity. Nat Rev Endocrinol. 2019;15(6):339–355. 10.1038/s41574-019-0170-1. [PubMed: 30814687]
5. Cabahug-Zuckerman P, Liu C, Cai C, et al. Site-specific load-induced expansion of sca-1+Prrx1+ and sca-1−Prrx1+ cells in adult mouse long bone is attenuated with age. JBMR Plus. 2019;3(9):e10199. [PubMed: 31667455]
6. Fafian-Labora J, Fernandez-Pernas P, Fuentes I, et al. Influence of age on rat bonemarrow mesenchymal stem cells potential. Sci Rep. 2015;5:16765. [PubMed: 26581954]
7. Razi H, Birkhold AI, Weinkamer R, Duda GN, Willie BM, Checa S. Aging leads to a dysregulation in mechanically driven bone formation and resorption. J Bone Min Res. 2015;30(10):1864–1873.
8. Bikle DD, Halloran BP, Morey-Holton E. Impact of skeletal unloading on bone formation: role of systemic and local factors. Acta Astronaut. 1994;33(0):119–129. [PubMed: 11539511]
9. Greenleaf JE, Bulbulian R, Bernauer EM, Haskell WL, Moore T. Exercise-training protocols for astronauts in microgravity. J Appl Physiol. 1989;67(6):2191–2204. [PubMed: 2691487]
10. Puts R, Albers J, Kadow-Romacker A, Geissler S, Raum K. Influence of donor age and stimulation intensity on osteogenic differentiation of rat mesenchymal stromal cells in response to focused low-intensity pulsed ultrasound. Ultrasound Med Biol. 2016;42(12):2965–2974. [PubMed: 27680572]
11. Maredziak M, Marycz K, Tomaszewski KA, Kornicka K, Henry BM. The influence of aging on the regenerative potential of human adipose derived mesenchymal stem cells. Stem cells Int. 2016;2016:2152435. [PubMed: 26941800]
12. Bas G, Loisate S, Hudon SF, et al. Low intensity vibrations augment mesenchymal stem cell proliferation and differentiation capacity during in vitro expansion. Sci Rep. 2020;10(1):9369. [PubMed: 32523117]
13. Touchstone H, Bryd R, Loisate S, et al. Recovery of stem cell proliferation by low intensity vibration under simulated microgravity requires intact LINC complex npj. Microgravity. 2019;5(11).
14. Hell RCR, Ocarino NM, Boeloni JN, et al. Physical activity improves age-related decline in the osteogenic potential of rats' bone marrow-derived mesenchymal stem cells. Acta Physiol. 2012;205(2):292–301.
15. Singulani MP, Stringhetta-Garcia CT, Santos LF, et al. Effects of strength training on osteogenic differentiation and bone strength in aging female Wistar rats. Sci Rep. 2017;7:42878. [PubMed: 28211481]
16. Rubin CT, Lanyon LE. Regulation of bone mass by mechanical strain magnitude. Calcif Tissue Int. 1985;37(4):411–417. [PubMed: 3930039]
17. O'Connor JA, Lanyon LE, MacFie H. The influence of strain rate on adaptive bone remodelling. J Biomech. 1982;15(10):767–781. [PubMed: 7153230]

18. Rath B, Nam J, Knobloch TJ, Lannutti JJ, Agarwal S. Compressive forces induce osteogenic gene expression in calvarial osteoblasts. J Biomech. 2008;41(5):1095–1103. [PubMed: 18191137]
19. Poliachik SL, Threet D, Srinivasan S, Gross TS. 32 wk old C3H/HeJ mice actively respond to mechanical loading. Bone. 2008;42(4):653–659. [PubMed: 18280231]
20. Rubin C, Turner AS, Bain S, Mallinckrodt C, McLeod K. Anabolism. Low mechanical signals strengthen long bones. Nature. 2001;412(6847):603–604.
21. Oxlund BS, Ortoft G, Andreassen TT, Oxlund H. Low-intensity, high-frequency vibration appears to prevent the decrease in strength of the femur and tibia associated with ovariectomy of adult rats. Bone. 2003;32(1):69–77. [PubMed: 12584038]
22. Tanaka SM, Li J, Duncan RL, Yokota H, Burr DB, Turner CH. Effects of broad frequency vibration on cultured osteoblasts. J Biomech. 2003;36(1):73–80. [PubMed: 12485640]
23. Garman R, Gaudette G, Donahue LR, Rubin C, Judex S. Low-level accelerations applied in the absence of weight bearing can enhance trabecular bone formation. J Orthop Res official Publ Orthop Res Soc. 2007;25(6):732–740.
24. Wren TA, Lee DC, Hara R, et al. Effect of high-frequency, low-magnitude vibration on bone and muscle in children with cerebral palsy. J Pediatr Orthop. 2010;30(7):732–738. [PubMed: 20864862]
25. Pre D, Ceccarelli G, Gastaldi G, et al. The differentiation of human adipose-derived stem cells (hASCs) into osteoblasts is promoted by low amplitude, high frequency vibration treatment. Bone. 2011;49(2):295–303. [PubMed: 21550433]
26. McGarry JG, Klein-Nulend J, Mullender MG, Prendergast PJ. A comparison of strain and fluid shear stress in stimulating bone cell responses–a computational and experimental study. Faseb J official Publ Fed Am Soc Exp Biol. 2005;19(3):482–484.
27. Sikavitsas VI, Bancroft GN, Holtorf HL, Jansen JA, Mikos AG. Mineralized matrix deposition by marrow stromal osteoblasts in 3D perfusion culture increases with increasing fluid shear forces. Proc Natl Acad Sci U S A. 2003;100(25):14683–14688. [PubMed: 14657343]
28. Bancroft GN, Sikavitsas VI, van den Dolder J, et al. Fluid flow increases mineralized matrix deposition in 3D perfusion culture of marrow stromal osteoblasts in a dose-dependent manner. Proc Natl Acad Sci USA. 2002;99(20):12600–12605. [PubMed: 12242339]
29. Weinbaum S, Cowin SC, Zeng Y. A model for the excitation of osteocytes by mechanical loading-induced bone fluid shear stresses. J Biomech. 1994;27(3):339–360. [PubMed: 8051194]
30. Reich KM, Gay CV, Frangos JA. Fluid shear stress as a mediator of osteoblast cyclic adenosine monophosphate production. J Cell Physiol. 1990;143(1):100–104. [PubMed: 2156870]
31. Qin YX, Hu M. Intramedullary pressure induced by dynamic hydraulic pressure stimulation and its potential in treatment of osteopenia. Bone. 2011;48:S186. S186.
32. Qin YX, Lam HY. Intramedullary pressure and matrix strain induced by oscillatory skeletal muscle stimulation and its potential in adaptation. J Biomech. 2009;42(2):140–145. [PubMed: 19081096]
33. Zhang P, Su M, Liu YL, Hsu A, Yokota H. Knee loading dynamically alters intramedullary pressure in mouse femora. Bone. 2007;40(2):538–543. [PubMed: 17070127]
34. Birks S, Uzer G. At the nuclear envelope of bone mechanobiology. Bone. 2021;151:116023. [PubMed: 34051417]
35. Price C, Zhou X, Li W, Wang L. Real-time measurement of solute transport within the lacunar-canalicular system of mechanically loaded bone: direct evidence for load-induced fluid flow. J Bone Min Res. 2011;26(2):277–285.
36. Vainionpaa A, Korpelainen R, Vihriala E, Rinta-Paavola A, Leppaluoto J, Jamsa T. Intensity of exercise is associated with bone density change in premenopausal women. Osteoporos Int a journal established as result of cooperation between the European Foundation for Osteoporosis and the National Osteoporosis Foundation of the USA. 2006;17(3):455–463.
37. Dickerson DA, Sander EA, Nauman EA. Modeling the mechanical consequences of vibratory loading in the vertebral body: microscale effects. Biomechanics Model Mechanobiol. 2008;7(3):191–202.
38. Chan ME, Uzer G, Rubin C. The potential benefits and inherent risks of vibration as a non-drug therapy for the prevention and treatment of osteoporosis. Curr Osteoporos Rep. 2013:1–9. [PubMed: 23275231]

39. Fritton SP, McLeod KJ, Rubin CT. Quantifying the strain history of bone: spatial uniformity and self-similarity of low-magnitude strains. J Biomech. 2000;33(3):317–325. [PubMed: 10673115]
40. Marin-Cascales E, Alcaraz PE, Ramos-Campo DJ, Martinez-Rodriguez A, Chung LH, Rubio-Arias JA. Whole-body vibration training and bone health in postmenopausal women: a systematic review and meta-analysis. Medicine. 2018;97(34):e11918. [PubMed: 30142802]
41. Gilsanz V, Wren TA, Sanchez M, Dorey F, Judex S, Rubin C. Low-level, high-frequency mechanical signals enhance musculoskeletal development of young women with low BMD. J.Bone Miner.Res. 2006;21(9):1464–1474. [PubMed: 16939405]
42. Ritzmann R, Stark C, Krause A. Vibration therapy in patients with cerebral palsy: a systematic review. Neuropsychiatric Dis Treat. 2018;14:1607–1625.
43. Mogil RJ, Kaste SC, Ferry RJ Jr, et al. Effect of low-magnitudeHigh-Frequency Mechanical Stimulation on BMD Among Young Childhood Cancer Survivors: A Randomized Clinical Trial. JAMA Oncol. 2016;2(7):908–914. [PubMed: 26967465]
44. Rubin C, Turner AS, Muller R, et al. Quantity and quality of trabecular bone in the femur are enhanced by a strongly anabolic, noninvasive mechanical intervention. J Bone Min Res. 2002;17(2):349–357.
45. Rubin C, Xu G, Judex S. The anabolic activity of bone tissue, suppressed by disuse, is normalized by brief exposure to extremely low-magnitude mechanical stimuli. Faseb J. 2001;15(12):2225–2229. [PubMed: 11641249]
46. Pongkitwitoon S, Uzer G, Rubin J, Judex S. Cytoskeletal configuration modulates mechanically induced changes in mesenchymal stem cell osteogenesis, morphology, and stiffness. Sci Rep. 2016;6:34791. [PubMed: 27708389]
47. Uzer G, Thompson WR, Sen B, et al. Cell mechanosensitivity to extremely low-magnitude signals is enabled by a LINCed nucleus. STEM CELLS. 2015;33(6):2063–2076. [PubMed: 25787126]
48. Uzer G, Pongkitwitoon S, Ete Chan M, Judex S. Vibration induced osteogenic commitment of mesenchymal stem cells is enhanced by cytoskeletal remodeling but not fluid shear. J Biomech. 2013;46(13):2296–2302. [PubMed: 23870506]
49. Uzer G, Bas G, Sen B, et al. Sun-mediated mechanical LINC between nucleus and cytoskeleton regulates betacatenin nuclear access. J Biomech. 2018;74:32–40. [PubMed: 29691054]
50. Thompson M, Woods K, Newberg J, Oxford JT, Uzer G. Low-intensity vibration restores nuclear YAP levels and acute YAP nuclear shuttling in mesenchymal stem cells subjected to simulated microgravity. NPJ microgravity. 2020;6(1):35. [PubMed: 33298964]
51. Newberg JK, Schimpf J, Woods K, Davis PH, Uzer G. Isolated nuclei stiffen in response to low intensity vibration. bioRxiv. 2020;111:110012. 10.1016/j.jbiomech.2020.110012.
52. Coughlin TR, Niebur GL. Fluid shear stress in trabecular bone marrow due to low-magnitude high-frequency vibration. J Biomech. 2012;45(13):2222–2229. [PubMed: 22784651]
53. Birmingham E, Kreipke TC, Dolan EB, et al. Mechanical stimulation of bone marrow in situ induces bone formation in trabecular explants. Ann Biomed Eng. 2015;43(4):1036–1050. [PubMed: 25281407]
54. Uzer G, Manske S, Chan M, et al. Separating fluid shear stress from acceleration during vibrations in vitro: identification of mechanical signals modulating the cellular response. Cell Mol Bioeng. 2012;5(3):266–276. [PubMed: 23074384]
55. Uzer G, Pongkitwitoon S, Ian C, et al. Gap junctional communication in osteocytes is amplified by low intensity vibrations in vitro. PLoS ONE. 2014;9(3):e90840. [PubMed: 24614887]
56. Glatt V, Canalis E, Stadmeyer L, Bouxsein ML. Age-related changes in trabecular architecture differ in female and male C57BL/6J mice. J Bone Miner Res official J Am Soc Bone Mineral Res. 2007;22(8):1197–1207.
57. Silva D, Kaduri M, Poley M, et al. Biocompatibility, biodegradation and excretion of polylactic acid (PLA) in medical implants and theranostic systems. Chem Eng J. 2018;340.
58. Tack P, Victor J, Gemmel P, Annemans L. 3D-printing Techniques in a Medical Setting: A Systematic Literature Review. 2016:15.
59. Xu X, Jha A, Harrington D, Farach-Carson M, Jia X. Hyaluronic acid-based hydrogels: from a natural polysaccharide to complex networks. Soft matter. 2012;8:3280–3294. [PubMed: 22419946]

60. Rubin CT, Lanyon LE. Regulation of bone formation by applied dynamic loads. J bone Jt Surg. Am volume. 1984;66(3):397–402.
61. Gurkan UA, Akkus O. The Mechanical Environment of Bone Marrow: A Review. 2008:36.
62. Jansen LE, Birch NP, Schiffman JD, Crosby AJ, Peyton SR. Mechanics of Intact Bone Marrow. vol. 50. 2015.
63. Rammohan AV, Lee T, Tan VBC. A novel morphological model of trabecular bone based on the gyroid. International Journal of Applied Mechanics. 2015;7(3):1550048.
64. Birks S, Howard S, O'Rourke C, Thompson WR, Lau A, Uzer G. Osterix-driven LINC complex disruption in vivo diminishes bone microarchitecture in 8-week male mice but not after 6-week voluntary wheel running. bioRxiv. 2023;42. 10.1002/jor.25849, 2023.08.24.554623.
65. Blaber J, Adair B, Antoniou A. Ncorr: open-source 2D digital image correlation matlab software. Exp Mech. 2015;55(6):1105–1122.
66. Ravikumar N, Noble C, Cramphorn E, Taylor ZA. A constitutive model for ballistic gelatin at surgical strain rates. J Mech Behav Biomed Mater. 2015;47:87–94. [PubMed: 25863009]
67. Papageorgiou M, Föger-Samwald U, Wahl K, Kerschan-Schindl K, Pietschmann P. Age- and strain-related differences in bone microstructure and body composition during development in inbred male mouse strains. Calcif Tissue Int. 2020;106(4):431–443. [PubMed: 31901965]
68. Sablatura LK, Tellman TV, Kim A, Farach-Carson MC. Bone marrow endothelial cells increase prostate cancer cell apoptosis in 3D triculture model of reactive stroma. Biology. 2022;11(9):1271. [PubMed: 36138750]
69. Lassen NE, Andersen TL, Pløen GG, et al. Coupling of bone resorption and formation in real time: new knowledge gained from human haversian BMUs. J Bone Min Res. 2017;32(7):1395–1405.
70. Delaisse JM, Andersen TL, Kristensen HB, Jensen PR, Andreasen CM, Søe K. Rethinking the bone remodeling cycle mechanism and the origin of bone loss. Bone. 2020;141:115628. [PubMed: 32919109]
71. Dupont S, Morsut L, Aragona M, et al. Role of YAP/TAZ in mechanotransduction. Nature. 2011;474(7350):179–183. [PubMed: 21654799]

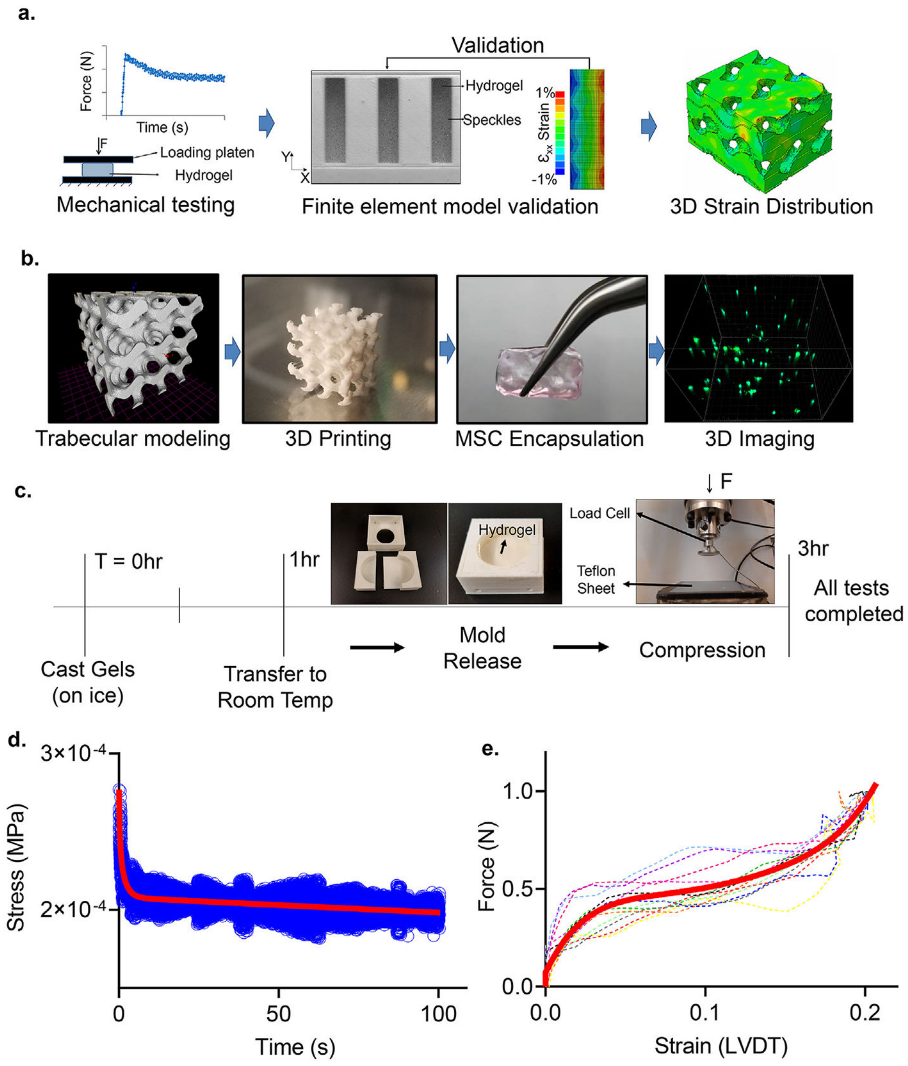

Fig. 1.

a) Both calibration and HA gels were mechanically tested and Finite element (FE) models were experimentally calibrated to generate 3D strain distributions scaffolds with both 13 % and 25 % trabecular bone volumes – representing bone volumes of 64 week old (aged) and 8 week old (young) adult male C57BL/6 J mouse. **b)** 3D bone analogs were generated using PLA printed trabeculae and primary MSCs were encapsulated using HA hydrogels with integrin binding motifs and metalloproteinases-sensitive crosslinkers. LIV was applied for 14 days (100 Hz, 1 g, 1hr/day) followed by volumetric imaging of scaffolds via confocal microscopy. **c)** Timeline of the compression testing, with all tests completed within 3 h of initial gelation for the calibration gels. 3D printed mold used to cast instantaneous gel pucks (24 mm internal diameter, and a height of 9 mm). Experiments were completed using an INSTRON ElectroPuls E10000 using a 10 N load-cell. The sample rested on a Teflon coated sheet lightly coated in water to prevent adherence. **d)** Relaxation data over a 100 s time period (blue) and the resulting fit line (red) relaxing from 2.8×10^{-5} MPa and reaching long term relaxation at approximately 2.1×10^{-5} Mpa. **e)** Instantaneous ramp data from 12 trials (dotted 5th order polynomial fit (blue), compressed to 0.2 strain (10.8 mm/s).

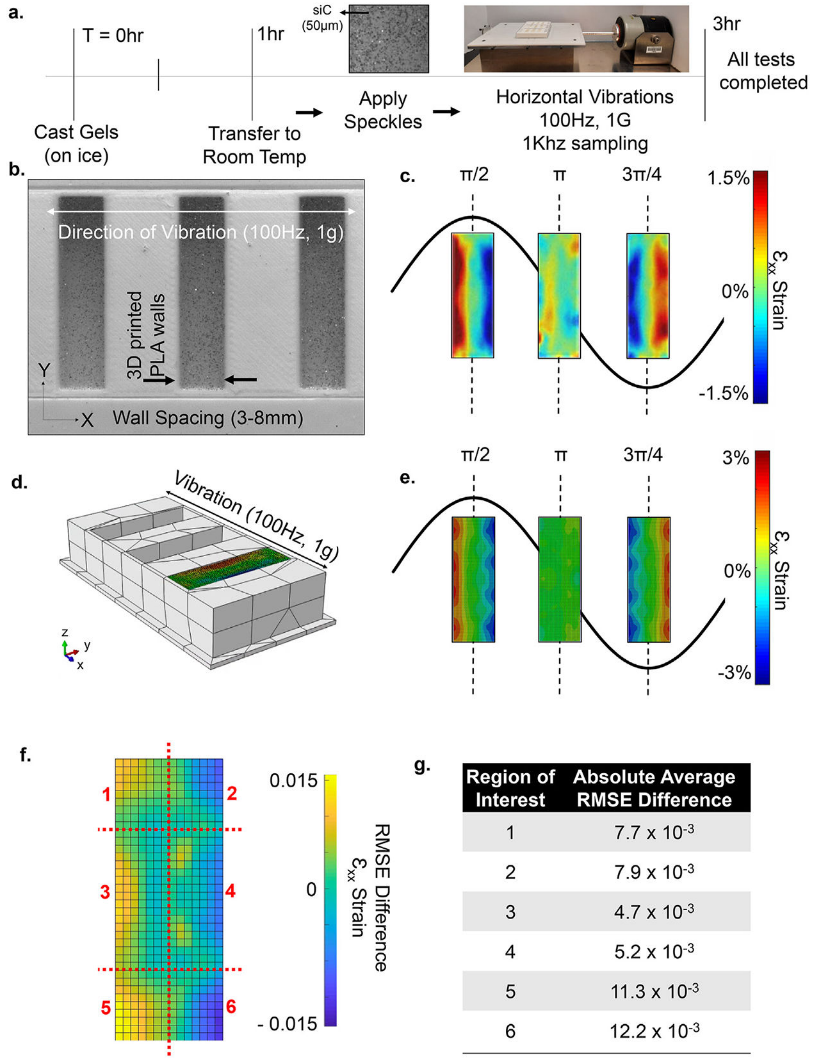

Region of Interest	Absolute Average RMSE Difference
1	7.7×10^{-3}
2	7.9×10^{-3}
3	4.7×10^{-3}
4	5.2×10^{-3}
5	11.3×10^{-3}
6	12.2×10^{-3}

Fig. 2.

a) Timeline of the DIC tests, with all tests completed within 3 h of initial gelation for the calibration gels. Hydrogels were speckled with 220 grid SiC and the camera recorded the motions at 2000 frames per second (fps). Horizontal vibration plate was driven by Labworks ET-126HF-1,-4 (13lbf) Electrodynamic transducer **b)** A PLA experimental setup was manufactured to visualize strain during100 Hz −1 g vibrations at the horizontal (X−) direction. **c)** ε_{xx} strains varied periodically with the maximum value of 0.015 at 8 mm spacing. **d)** Optimized finite Element (FE) model setup with 8 mm wall spacing. Wells were vibrated identically to the speckle experiments with each FE run was proceeded by a gravity step. **e)** ε_{xx} strain magnitude over the cycle. Maximum ε_{xx} values were symmetrical at both the $\pi / 2$ and $3\pi / 2$, in addition to both ends of the well, demonstrating steady state. **f)** The difference between the surface of DIC experimental and the FE model was measured with a 15 × 37 grid and divided into 6 regions for comparison. Most of the difference occurs on the outside, especially the outer edges. **g)** Largest difference of 0.015 of averaged ε_{xx} magnitude difference occurs in the regions 5 and 6. Regions 3 and 4 are the closest matching, with an averaged ε_{xx} magnitude difference of 0.0047 and 0.0052, respectively. The corner regions (1, 2, 5 and 6) has an averaged ε_{xx} magnitude difference of 0.0077, 0.0079, 0.0113, and 0.0122, respectively.

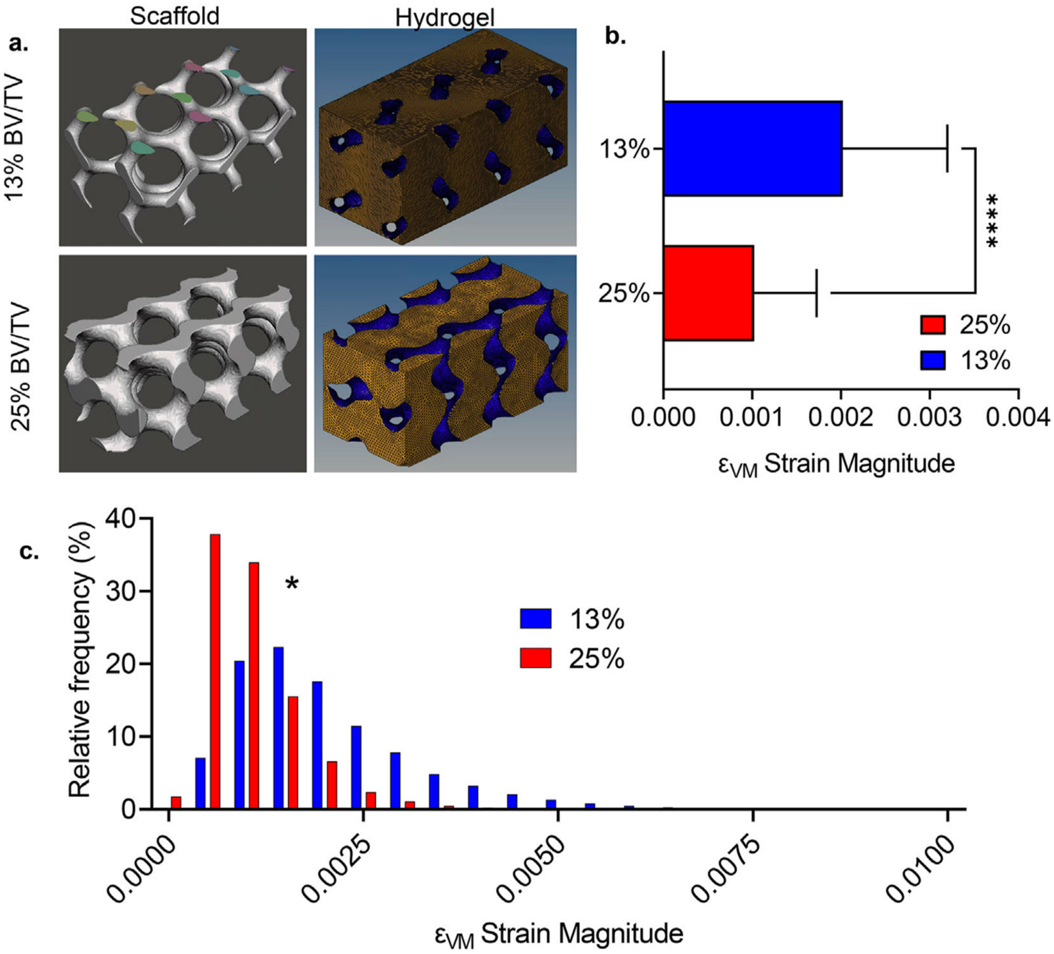

Fig. 3.

a) We compared the 3D strain distribution between 13 % and 25 % scaffolds under LIV using HA gel mechanical properties (Table S1). **b)** Comparing the Von Mises strain (ε_{VM}) magnitude averaged over steady–state cycles showed that εVM of 13 % was almost doubled compared to 25 % scaffold ($p < 0.0001$). **c)** ε_{VM} distribution indicated normally distributed strains for both 13 % and 25 % scaffolds. Histograms of 25 % and 13 % scaffolds were statistically different ($p < 0.05$). 25 % scaffold had more elements with lower strain values while 13 % scaffold showed elements with higher ε_{VM} strains.

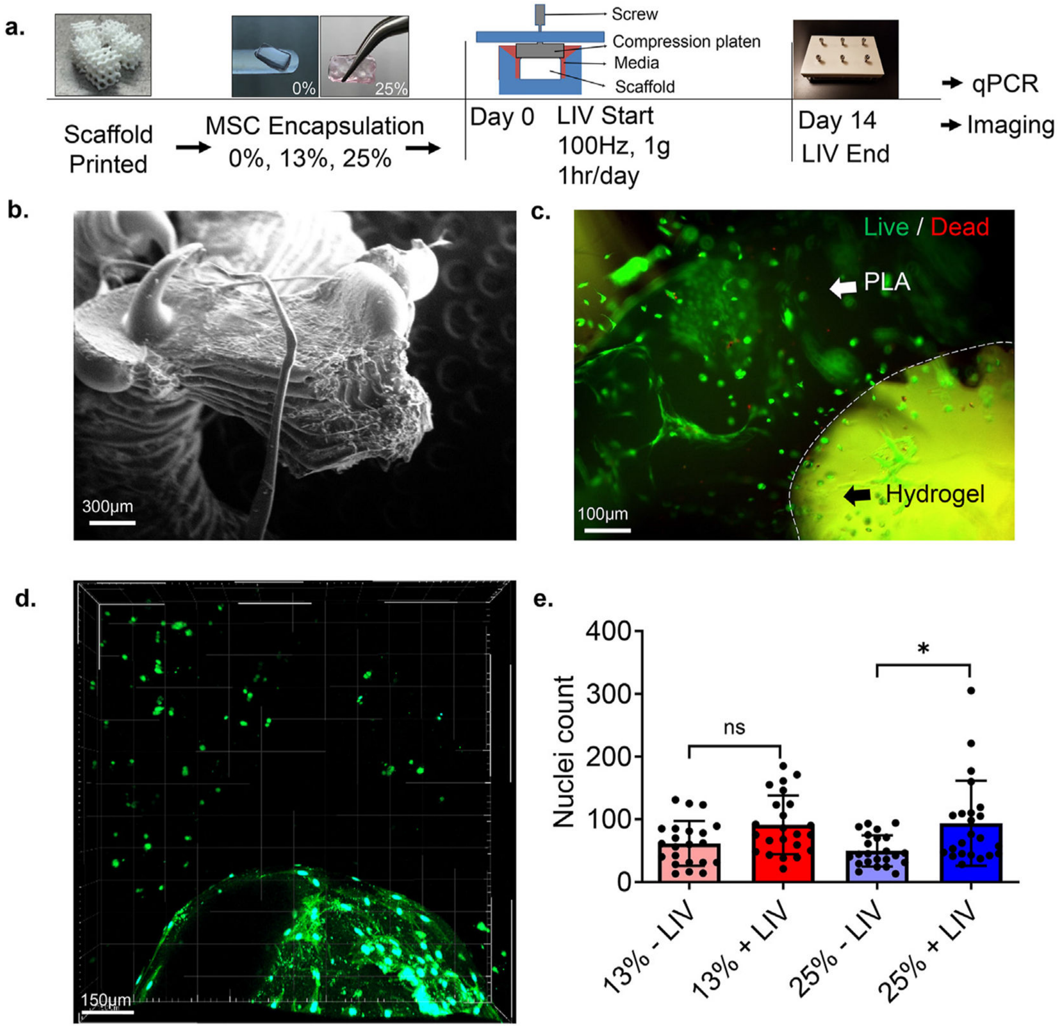

Fig. 4.

a) Two sets of PLA scaffolds (13 % and 25 % volume fill) and 0 % controls were generated. Cell-laden 13 % and 25 % scaffolds were vibrated 1 h every day at room temperature using 100 Hz frequency and 1 g acceleration magnitude outside of the incubator. After 14 days, samples were allocated for qPCR (N = 4 scaffolds/group), imaging (N = 3 scaffolds/group) **b)** PLA surface provides an ideal surface for cell attachment **c)** Utilizing live/dead straining to detect cell viability prior to start of the experiments at 7 days post-encapsulation showed viable cells on both PLA and in hydrogels. **d)** Morphology of cells on PLA surfaces was similar to cells on 2D culture plates (Fig. S4), showing elongated morphology while cells in hydrogels were smaller and more rounded. Due to difficulties of quantifying cells ion scaffold surface both imaging and RNA outcomes were measured in the hydrogel fraction. **e)** Nuclei counts averaged over each ROI were not statistically different from each other when compared between 13 % and 25 % under no-LIV conditions (61 vs 49). While 13 % and 25 % under LIV were also not statistically different (91 vs 94), application of LIV increased the nuclei count by 49 % in 13 % scaffolds (61–91, ns) and by 91 % in 25 % scaffolds (49–94, $p < 0.05$) when compared to no-LIV controls.

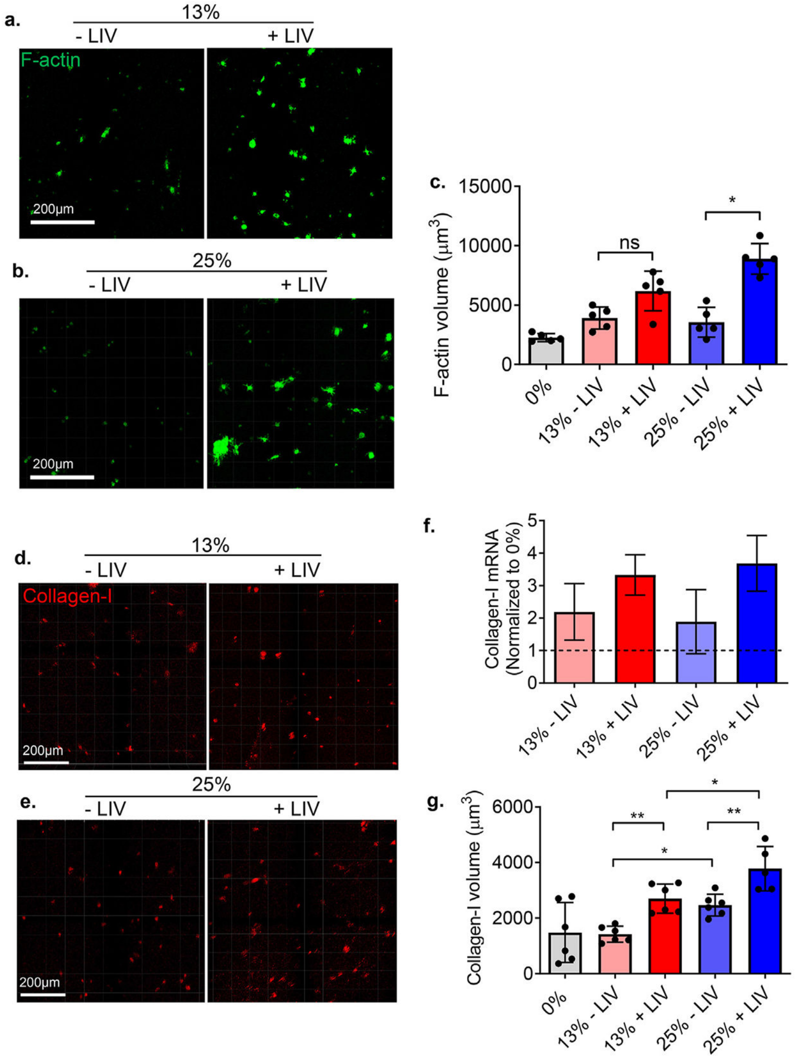

Fig. 5.

F-actin staining in cells in **a)** 13 % and **b)** 25 % scaffolds show increased F-actin volume in +LIV samples when compared to controls (−LIV). **c)** Quantification F-actin volume showed no change in −LIV groups. 13 % +LIV groups trended toward increased F-actin and 25 % +LIV group showed 2.5-fold increase in F-actin volume ($p < 0.05$). Collagen-I immunostaining in **d)** 13 % and **e)** 25 % scaffolds show increased collagen labeling in vibrated samples (+LIV), vs non vibrated controls (−LIV). **f)** Collagen-I mRNA quantification show an increasing trend of collagen-I levels in +LIV samples (+50 % in 13 % and +94 % in 25 % samples. All samples were normalized to 0 % controls (dashed gray bar) **g)** Quantification of collagen-I volume showed unchanged basal collagen-I levels between 0 % and 13 % controls while -LIV 25 % group showed a 73 % increase compared to -LIV 13 % group ($p < 0.05$). LIV increased collagen-I in both 13 % and 25 % groups by 87 % and 53 % respectively ($p < 0.01$) and +LIV 25 % remained significantly higher compared to + LIV 13 % group (37 %, $p < 0.05$).

Table 1

DOE factors used to minimize RMSE between *in vitro* and *in silico* results for calibration gels.

Stiffness	**Friction**	**Damping**	**RMSE**
1.5	10	0.3	0.41
1.5	10	0.003	0.37
1.5	10	0.03	0.47
1.5	0.1	0.3	0.50
1.5	0.1	0.003	0.38
1.5	0.1	0.03	0.38
1.5	0.75	0.3	0.35
1.5	0.75	0.003	0.36
1.5	0.75	0.03	0.36
0.5	10	0.3	0.53
0.5	10	0.003	0.45
0.5	10	0.03	0.56
0.5	0.1	0.3	0.58
0.5	0.1	0.003	0.50
0.5	0.1	0.03	0.49
0.5	0.75	0.3	0.63
0.5	0.75	0.003	0.64
0.5	0.75	0.03	0.63
1	10	0.3	0.29
1	10	0.003	0.28
1	10	0.03	0.28
1	0.1	0.3	0.16
1	0.1	0.003	0.16
1	0.1	0.03	0.16
1	0.75	0.3	0.30
1	0.75	0.003	0.28
1	0.75	0.03	0.19

Table 2

In silico comparison of directional strains between 13 % and 25 % scaffolds during LIV.

Tensor	**13 %**		**25 %**	
	Min	**Max**	**Min**	**Max**
XX	−0.053	0.062	−0.047	0.012
YY	−0.056	0.071	−0.017	0.050
ZZ	−0.075	0.067	−0.047	0.029
XY	−0.102	0.067	−0.023	0.025
YZ	−0.082	0.104	−0.042	0.053
ZX	−0.078	0.089	−0.021	0.062